

Layer Resolved Magnetotransport Properties in Antiferromagnetic/Paramagnetic Superlattices

Sandip Halder,¹ Sourav Chakraborty,^{1,2} and Kalpataru Pradhan¹

¹*Theory Division, Saha Institute of Nuclear Physics,*

A CI of Homi Bhabha National Institute, Kolkata-700064, India

²*Department of Condensed Matter and Materials Physics,*

S. N. Bose National Centre for Basic Sciences, JD Block, Sector III, Salt Lake, Kolkata-700106, India

We investigate the layer resolved magnetotransport properties of the antiferromagnetic/paramagnetic superlattices based on one band half-filled Hubbard model in three dimensions. In our set up the correlated layers (with on-site repulsion strength $U \neq 0$) are intercalated between the uncorrelated ($U = 0$) layers. Our calculations based on the semi-classical Monte-Carlo technique show that the magnetic moments are induced in the uncorrelated layers at low temperatures due to kinetic hopping of the carriers across the interface. The average induced magnetic moment in the uncorrelated layer varies nonmonotonically with the U values of the correlated layer. Interestingly, the induced magnetic moments are antiferromagnetically arranged in uncorrelated layers and mediates the antiferromagnetic ordering between correlated layers. As a result the whole SL system turns out to be antiferromagnetic insulating at low temperatures. For $U \sim$ bandwidth the local moments in the correlated planes increases as a function of the distance from the interface. Expectedly our in-plane resistivity calculations show that the metal insulator transition temperature of the central plane is larger than the edge planes in the correlated layers. On the other hand, although the induced moments in uncorrelated planes decreases considerably as move from edge planes to center planes the metal insulator transition temperature remains more or less same for all planes. The induced moments in uncorrelated layers gradually dissipates with increasing the thickness of uncorrelated layer and as a result the long range antiferromagnetic ordering vanishes in the superlattices similar to the experiments.

I. INTRODUCTION

Correlated transition metal oxide heterostructures are extensively studied nowadays due to their unusual intriguing interfacial properties^{1–11}. Various reconstructions such as electronic^{12–15}, magnetic^{16,17}, orbitals^{18–24} and structural reconstructions^{25–27} at the interface give rise to many fascinating and promising phenomena that are absent in the constituent bulk materials^{1,9,28–38}. These emerging phenomena like metallicity^{31,39}, magnetism^{32,40} and superconductivity^{33,41} and their coexistence^{42–44} in the $LaAlO_3/SrTiO_3$ heterostructures, metallicity in the interfaces of Mott insulator and band insulator^{34,45}, induced magnetism in the paramagnetic layers in magnetic/paramagnetic superlattices^{46–53}, and ferromagnetism at the interfaces of paramagnetic/paramagnetic superlattices³⁵ pose many elemental scientific questions that need to be addressed. Pinning down the underlying mechanism remains a challenging task for both theory and experiments and remains a subject of active research⁵⁴. A very good knowledge about the structural and/or the chemical complexity and the modulation of the elementary phases at the interfaces are crucial to design artificially new functional materials based on oxide heterostructures^{4,5}.

In $LaTiO_3/SrTiO_3$ (LTO/STO) superlattices (SL), where LTO is an antiferromagnetic Mott-insulator and STO is a nonmagnetic band insulator, an unexpected conducting and magnetic phase appears at the interfaces^{34,45}. As a matter of fact the electrochemical potential difference at the interface facilitate the leakage

of the charge from the filled LTO Ti- d band to the empty STO Ti- d band and promote the magnetic and conducting state at the interface¹². Interestingly, the amount of charge transfer across the interface can be controlled by the relative thickness of the STO layer⁵⁵. Induced magnetic moments are also observed in STO layer in $La_{0.7}Sr_{0.3}MnO_3/SrTiO_3$ (LSMO/STO) and $LaMnO_3/SrTiO_3$ (LMO/STO) SLs^{16,38}. These induced magnetic moments in Ti controls the overall magnetic and transport properties of the superlattice system when the thickness of the STO layer is less than 1 nm¹⁶. At the same time the thickness of LMO layer, due to the orbital reconstructions at the interface of LMO/STO superlattices^{38,55}, provides a new pathway to tune the interaction between the manganite and the titanate³⁸. Density functional theory studies of LMO/STO superlattices also show that the magnetic and electronic properties can be controlled by the thickness of the LMO and STO layers^{56,57}.

Charge transfer from the Mn to the Ni atoms also plays a vital role in LMO and LNO ($LaNiO_3$) superlattices^{47–53} in inducing magnetic moments in LNO layer. These induced magnetic moments drives a metal-insulator transition when the thickness of the LNO layers reduces to 2 unit cells or less^{11,46,51,58}. Superlattices comprised of doped Mott-Hubbard insulator $LaTiO_{3+\delta}$ and LNO also offers an unusual electronic structure at the interfaces facilitated by the charge transfer from Ti to Ni sites¹⁴. Consequently an insulating ground state along with orbital polarization and e_g orbital band splitting like mechanisms are observed at the interface. Further,

it is observed that the metal-insulator transition temperature decreases as one increases the width of the $LaNiO_3$ layer in $NdNiO_3/LaNiO_3$ SLs⁵⁹. On the other hand it is shown that the antiferromagnetic transition temperature decreases with decreasing the layer thickness of the antiferromagnetic $CeIn_3$ layer in $CeIn_3/LaIn_3$ (antiferromagnetic/metallic) SLs⁶⁰. In fact, the antiferromagnetic order vanishes when the thickness of $CeIn_3$ reaches as thin as 2 unit cells.

In NiO/Pd superlattices, a type of antiferromagnetic/paramagnetic superlattices, magnetization is induced in the interfacial metallic Pd layers due to the proximity effect of the AF NiO ^{61–65}. It is also observed that the induced magnetic moment in Pd layers decreases with distance from the interfaces and vanishes at a distance 35\AA away from interface⁶³. Induced magnetic moments are also observed in the metallic interfacial Cu layers in CuO/Cu (AF/PM) superlattices⁶⁶. Model Hamiltonian based calculations indicate that the magnetic moments are induced in the metallic layers due to the proximity of the AF insulating layers^{67–70}. In addition, it is also proposed that the metallicity penetrates in to the insulating AF layers⁶⁷, but details of the transport calculations are not provided. More and more theoretical studies are needed to understand the magnetotransport properties of magnetic/paramagnetic SLs.

Motivated by the fascinating experimental results in complex oxide superlattices we investigate the magnetotransport properties of the correlated/uncorrelated (antiferromagnetic/paramagnetic) superlattices. In order to explore various phenomena we analyze a range of 3D superlattices based on one band Hubbard model where correlated ($U \neq 0$) layers of width w_U and the uncorrelated ($U = 0$) layers of width w_0 are periodically arranged as shown in Fig. 1. At half-filling our uncorrelated layers mimics the paramagnetic metallic (PM-M) state where as the correlated layers imitate the antiferromagnetic insulating state (AF-I) layers. Overall, our study unveils the key role of mutual cooperation of the induced magnetic moments in the uncorrelated (paramagnetic) layers and the local moment in the correlated (antiferromagnetic) layers in establishing the antiferromagnetic insulating nature of the whole antiferromagnetic/paramagnetic superlattices. In addition, we emphasize that the induced moments in uncorrelated planes decreases considerably as a function of the distance from the interface. As a result the induced moments completely dissipates with increasing the thickness of uncorrelated layers and nullifies the antiferromagnetic ordering among correlated layers. We comprehensively show that the strength of the local moments and the metal-insulator transition temperature increases as one moves from the edge planes to the center plane in correlated layers.

We organize the paper in the following way: In section II we layout the model Hamiltonian associated with the correlated/uncorrelated superlattices and briefly discuss the numerical methodology. We outline different physical observables to study magnetotransport properties of

the antiferromagnetic/paramagnetic SLs in section III. Then in section IV we present the magnetic and transport properties and construct the $U - T$ phase diagrams for different $w_U/1$ superlattices. We establish the mutual cooperation between the magnetic ordering between the correlated and the uncorrelated layers in section V and present the plane resolved magnetic and transport properties of individual layers in section VI. In section VII we briefly analyze the $1/w_0$ SLs and then outline the $x - T$ phase diagram in section VII. We thoroughly study $3/3$ SL in section VII. At the end, we summarize our results in section X.

II. MODEL HAMILTONIAN AND METHOD

To study of the magnetotransport properties of antiferromagnetic/paramagnetic superlattices (SLs) we consider following electron-hole symmetric one orbital Hubbard model:

$$H = -t \sum_{\langle i,j \rangle, \sigma} (c_{i,\sigma}^\dagger c_{j,\sigma} + H.c.) + U \sum_i (n_{i,\uparrow} - \frac{1}{2})(n_{i,\downarrow} - \frac{1}{2}) - \mu \sum_i c_{i,\sigma}^\dagger c_{i,\sigma}$$

where $c_{i,\sigma}^\dagger$ ($c_{i,\sigma}$) is the electron creation (annihilation) operator at site i with spin σ (\uparrow or \downarrow) and t is the hopping amplitude between the nearest neighbors sites. In the second term U is the strength of on-site Coulomb repulsion between two electrons of opposite spin at site i and $n_{i,\sigma} = c_{i,\sigma}^\dagger c_{i,\sigma}$ is the spin sum occupation number operator at site i . μ is the chemical potential which controls the overall density of the system. In our electron-hole symmetric model Hamiltonian $\mu = 0$ for half-filling case. Then neglecting the constant term we write down the Hamiltonian in the following form:

$$H = -t \sum_{\langle i,j \rangle, \sigma} (c_{i,\sigma}^\dagger c_{j,\sigma} + H.c.) + U \sum_i n_{i,\uparrow} n_{i,\downarrow} - \frac{U}{2} \sum_i n_i = H_0 + H_{int}$$

where H_0 contains the one body part (i.e. quadratic terms) and H_{int} denotes the interacting part (i.e. quartic term) of the Hamiltonian. Now to solve the Hamiltonian using Monte Carlo method the quartic interaction term can be transformed into combination of two different quadratic terms to set up the Hubbard-Stratonovich (HS) decomposition:

$$U n_{i,\uparrow} n_{i,\downarrow} = U \left[\frac{1}{4} n_i^2 - (\mathbf{S}_i \cdot \hat{\Omega})^2 \right]$$

where $\mathbf{S}_i (= \frac{\hbar}{2} \sum_{\alpha,\beta} c_{i,\alpha}^\dagger \sigma_{\alpha,\beta} c_{i,\beta})$; σ are the Pauli matrices) is the spin at i^{th} site and $\hat{\Omega}$ is the arbitrary unit

vector. The partition function of the model Hamiltonian is written as $Z = Tr e^{-\beta(H_0 + H_{int})}$ where $\beta = 1/T$ and the Boltzmann constant k_B and \hbar are set to 1. The interval $[0, \beta]$ is divided into M equally spaced slices of width $\Delta\tau$ such that $\beta = M\Delta\tau$. For large values of M i.e. in the limit $\Delta\tau \rightarrow 0$, using Suzuki-Trotter transformation we can write $e^{-\beta(H_0 + H_{int})} = (e^{-\Delta\tau H_0} e^{-\Delta\tau H_{int}})^M$ up to first order in $\Delta\tau$. After that by implementing the Hubbard-Stratonovich transformation the interacting part of the partition function $e^{-\Delta\tau U \sum_i [\frac{1}{4} n_i^2 - (\mathbf{S}_i \cdot \hat{\Omega}_i)^2]}$ for a generic time slice ' l ' can be expressed as

$$\sim \int d\phi_i(l) d\Delta_i(l) d^2\Omega_i(l) \times e^{-\Delta\tau [\sum_i \{ \frac{\phi_i(l)^2}{2} + i\phi_i(l)n_i + \frac{\Delta_i(l)^2}{2} - 2\Delta_i(l)\hat{\Omega}_i(l) \cdot \mathbf{S}_i \}]}.$$

The auxiliary field $\phi_i(l)$ [$\Delta_i(l)$] introduced by the Hubbard-Stratonovich decomposition is coupled with the charge density n_i (spin vector \mathbf{S}_i). Now we define a new vector auxiliary field $\mathbf{m}_i(l) = \Delta_i(l)\hat{\Omega}_i(l)$. Finally we obtain the total partition function as

$$Z = const. \times Tr \prod_{l=M}^1 \int d\phi_i(l) d^3\mathbf{m}_i(l) \times e^{-\Delta\tau [H_0 + \sum_i \{ \frac{\phi_i(l)^2}{2} + i\phi_i(l)n_i + \frac{\mathbf{m}_i(l)^2}{2} - 2\mathbf{m}_i \cdot \mathbf{S}_i \}]}.$$

The product follows the time ordered product, where the time slice l runs from M to 1. From the partition function we can extract an effective Hamiltonian. At this moment we make two major approximations: (i) by freezing the τ dependence of the auxiliary fields and retaining the spatial fluctuations of the auxiliary fields, (ii) using the saddle point value of $i\phi_i(l) = \frac{U}{2} \langle n_i \rangle$. After all by redefining $\mathbf{m}_i \rightarrow \frac{U}{2} \mathbf{m}_i$, we obtain the following effective Hamiltonian^{71,72}:

$$H_{eff} = -t \sum_{\langle i,j \rangle, \sigma} (c_{i,\sigma}^\dagger c_{j,\sigma} + H.c.) + \frac{U}{2} \sum_i (\langle n_i \rangle n_i - \mathbf{m}_i \cdot \sigma_i) + \frac{U}{4} \sum_i (\mathbf{m}_i^2 - \langle n_i \rangle^2) - \frac{U}{2} \sum_i n_i - \mu \sum_i n_i. \quad (1)$$

We simulate the effective model Hamiltonian (H_{eff}) using semi-classical Monte Carlo (s-MC)⁷¹⁻⁷⁵ method by diagonalizing the fermionic sector in the background of fix $\{\mathbf{m}_i\}$ and $\{\langle n_i \rangle\}$ configurations. The classical $\{\mathbf{m}_i\}$ variables are updated by visiting every lattice site sequentially by implementing metropolis algorithm. We determine $\{\langle n_i \rangle\}$ self-consistently at every 10th step of the MC system sweep which is then used in the next 10 MC sweeps. We measure physical quantities at every 10th step after the thermal equilibrium to discard

illicit correlation in the data. We compute the effective Hamiltonian in a large system size $8 \times 8 \times 12$ with the help of travelling cluster approximation (TCA)⁷⁶⁻⁷⁹ based Monte Carlo technique using $4 \times 4 \times 8$ TCA cluster.

In the bulk system (where all the sites have finite U), the ground state remains in an antiferromagnetic insulating (AF-I) state for $U > 0$ and in a paramagnetic metallic (PM-M) state for $U = 0$, at half-filling. We have designed AF/PM (correlated/uncorrelated) superlattices (SLs) where the AF layer ($U \neq 0$) of width w_U and the PM layer ($U = 0$) of width w_0 are periodically arranged to form the superlattices. We call the superlattices as w_U/w_0 SLs, illustrated schematically in Fig. 1. We define $x (= \frac{w_U}{w_U + w_0})$ as the fraction of correlated planes in the w_U/w_0 SL.

III. PHYSICAL OBSERVABLES

We evaluate various physical observables to investigate the magnetotransport properties of the whole antiferromagnetic/paramagnetic superlattices. For all superlattices we calculate the layer resolved (separately for correlated layers and uncorrelated layers) observables. In some cases we also calculate plane resolved properties of a given layer (correlated or uncorrelated).

The system averaged magnetization squared is calculated as $M = \langle (n_\uparrow - n_\downarrow)^2 \rangle = \langle n \rangle - 2\langle n_\uparrow n_\downarrow \rangle$ where $\langle n \rangle = \langle n_\uparrow + n_\downarrow \rangle$. The average magnetic moment irrespective of its direction is inferred from this indicator M . The angular brackets represent quantum mechanical and thermal averages throughout the Monte Carlo generated equilibrium configurations. To analyze the long range antiferromagnetic order in superlattices we calculate the structure factor $S(\mathbf{q})$ for $\mathbf{q} = (\pi, \pi, \pi)$ as follows:

$$S(\mathbf{q}) = \frac{1}{N^2} \sum_{i,j} \langle \mathbf{S}_i \cdot \mathbf{S}_j \rangle e^{i\mathbf{q} \cdot (\mathbf{r}_i - \mathbf{r}_j)}$$

where N is the total number of sites of the system and i and j run all over the sites of the system. We also calculate the specific heat of the system by differentiating the total energy with respect to temperature, $C_v(U, T) = \frac{dE(U, T)}{dT}$. We apply central difference formula to evaluate the specific heat numerically.

Density of states (DOS) of the system at frequency ω is determined by using the expression $D(\omega) = \sum_\alpha \delta(\omega - \epsilon_\alpha)$, where ϵ_α are the single particle eigen values and α runs over the total number ($= 2N$) of eigen values of the system. In our simulation, Lorentzian representation of the delta function with broadening $\sim BW/2N$ (BW is the bare bandwidth) is applied to evaluate the DOS.

The longitudinal (along z -axis) and transverse (along x -axis) resistivity of the superlattice are calculated by using dc limit of the optical conductivity through Kubo-Greenwood formalism^{77,80,81}, represented by

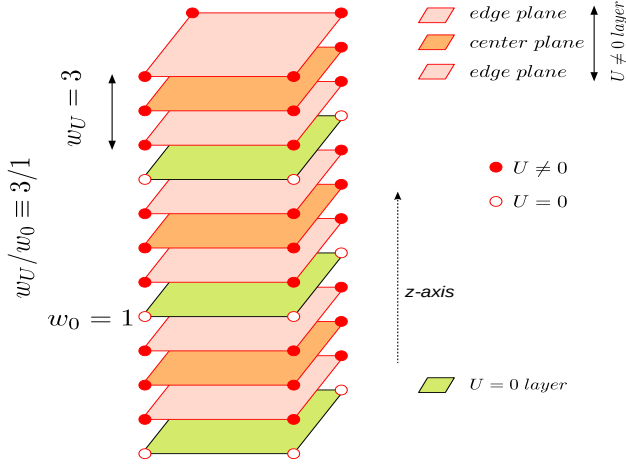


FIG. 1: Schematic view of the superlattice system. Red filled (open) circles represent the correlated (uncorrelated) sites with $U \neq 0$ ($U = 0$). The width of the correlated (uncorrelated) layer is w_U (w_0) i.e. it contains w_U (w_0) number of planes. These correlated and uncorrelated layers are periodically arranged along the z -axis and denoted as w_U/w_0 SL. The edge and center planes of the correlated layer are represented by different colors. Total width of the superlattice along the z -axis is fixed; $L_z = 12$. In this schematic of $3/1$ SL $w_U/w_0 \equiv 3/1$ and $3 \times (w_U + w_0) = 12$.

$$\sigma(\omega) = \frac{A}{N} \sum_{\alpha, \beta} (n_{\alpha} - n_{\beta}) \frac{|f_{\alpha\beta}|^2}{\epsilon_{\beta} - \epsilon_{\alpha}} \delta[\omega - (\epsilon_{\beta} - \epsilon_{\alpha})]$$

where $A = \pi e^2 / \hbar a$ (a is the lattice parameter). $f_{\alpha\beta}$ represents the matrix elements of the current operator $\hat{j}_z = it \sum_{i, \sigma} (c_{i, \sigma}^{\dagger} c_{i+z, \sigma} - c_{i+z, \sigma}^{\dagger} c_{i, \sigma})$ or, $\hat{j}_x = i \sum_{i, \sigma} (c_{i, \sigma}^{\dagger} c_{i+x, \sigma} - c_{i+x, \sigma}^{\dagger} c_{i, \sigma})$ between the eigen states $|\psi_{\alpha}\rangle$ and $|\psi_{\beta}\rangle$ with corresponding eigen energies ϵ_{α} and ϵ_{β} , respectively and $n_{\alpha} = \theta(\mu - \epsilon_{\alpha})$ is the Fermi function associated with the single particle energy level ϵ_{α} . Afterwards the dc conductivity is computed by averaging over the low-frequency interval as follows:

$$\sigma_{av}(\Delta\omega) = \frac{1}{\Delta\omega} \int_0^{\Delta\omega} \sigma(\omega) d\omega$$

where $\Delta\omega$ is selected three to five times larger than the average eigen value separation of the system, defined as the ratio of the bare bandwidth to the total number of eigen values. All the physical parameters like U , T , ω are measured in units of t .

IV. $U - T$ PHASE DIAGRAMS FOR VARIOUS SUPERLATTICES

First we briefly discuss the physics of the bulk system ($U \neq 0$ for all the sites) before analyzing the intriguing phenomena in AF/PM superlattices. We present the

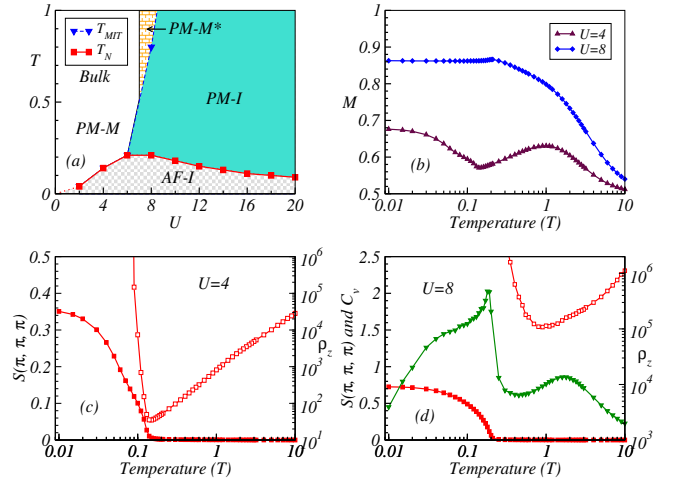


FIG. 2: (a) $U - T$ phase diagram of the bulk system ($U \neq 0$ for all the sites). The system directly converts to an AF-I state from a PM-M state for $U < 8$. A PM-I phase intervenes between the PM-M* and the AF-I phases for $U \geq 8$. For details about the characterization of these phases please see the text. (b) The local magnetic moment M (for $U = 8$) increases with decreasing temperature and saturates at low temperature, displaying a small peak near T_N . For $U = 4$, M_U decreases from $T \sim 1$ down to $T \sim T_N$ and then starts to increase below T_N . (c) Temperature dependence of $S(\pi, \pi, \pi)$ (left axis) and ρ_z (right axis) for $U = 4$ show that the antiferromagnetic transition and the metal-insulator transition occur simultaneously at the same temperature (i.e. $T_N = T_{MIT}$). (d) For $U = 8$ the T_{MIT} is larger than T_N and as a result PM-I phase appears between the PM-M* and the AF-I phases as shown in (a). The high-T C_v peak is consistent with the metal-insulator transition, while the low-T C_v peak corresponds to the antiferromagnetic transition.

$U - T$ phase diagram for bulk system in Fig. 2(a). The ground state of the bulk system shows a G-type antiferromagnetic (G-AF) insulating phase at low temperatures for all U values. Please notice that the Neel temperature (T_N) varies nonmonotonically with U values. Specifically, T_N increases with U up to $U = 8$ and decreases thereafter. For $U < 8$ the system transits from a paramagnetic metallic (PM-M) phase to an AF insulating phase (AF-I) with decreasing the temperature and the metal insulator transition temperature (T_{MIT}) coincides with the T_N . On the other hand, for $U = 8$ or more the system encounters a paramagnetic insulating (PM-I) region above the T_N . As we increase the temperature further the system crosses over to a slightly different kind of paramagnetic metallic phase (abbreviated as PM-M*) above T_{MIT} (denoted by dashed line). In order to characterize the properties of PM-M (for $U \leq 6$) and PM-M* (for $U \geq 8$) phases we focus on the M vs T plot (see Fig. 2(d)). In PM-M* phase (for $U = 8$ case), the magnetic moment M increases with decreasing temperature whereas the magnetic moment M decreases in the PM-M phase (for $U = 4$ case) as we go below $T = 1$ down to T_N in our phase diagram. In other words local magnetic moments

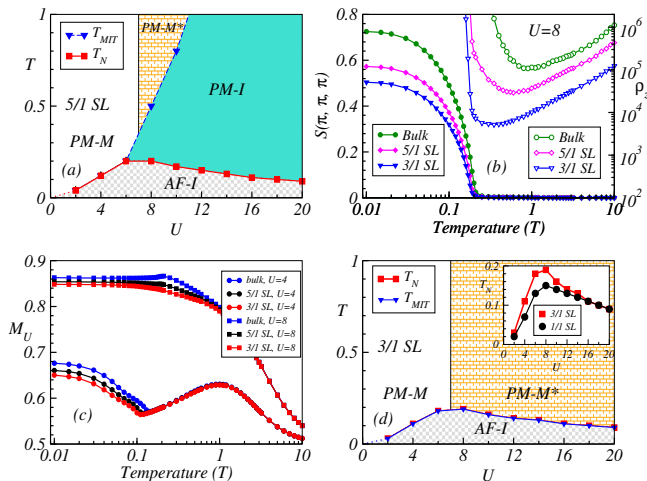


FIG. 3: (a) The $U - T$ phase diagram of the 5/1 superlattice: Area of the PM-I phase shrinks whereas the metallic phase (PM-M*) gets enlarged as compared to the bulk system phase diagram. (b) Temperature dependence of $S(\pi, \pi, \pi)$ (left axis) and ρ_z (right axis) are plotted for bulk ($x = 1$), 5/1 SL ($x \sim 0.83$) and 3/1 ($x = 0.75$) SL for $U = 8$. The T_{MIT} decreases as we move from bulk to 5/1 to 3/1 SL whereas the T_N s remain more or less same. The T_{MIT} matches with the T_N only for 3/1 SL. (c) Temperature evolution of the local moments in the correlated layers (M_U) are plotted for bulk, 5/1 and 3/1 SLs using two different U values ($U = 4$ and 8). Low temperature saturation magnetic moment increases as one moves from 3/1 SL to 5/1 SL to bulk systems. For $U = 4$ a dip near the T_N is present in all three systems. (d) The PM-I phase disappears in $U - T$ phase diagram for 3/1 SL. The PM-I phase is covered-up by PM-M* phase. The 3/1 SL directly transforms from PM-M (or PM-M*) state to AF-I state. For more details please see the texts.

are performed in PM-M* phase at high temperatures (~ 1) unlike the PM-M phase. Although not necessary, we differentiate PM-M and PM-M* phases in the phase diagram for brevity, which will be useful in discussing the phase diagrams of SL systems.

We plot the magnetic and transport properties in Fig. 2(b)-(d) that we used to set up the $U - T$ phase diagram presented in Fig. 2(a). Mainly, we focus on two U values ($U = 4$ and 8) which represent two different regimes in our $U - T$ phase diagram. As we mentioned earlier the structure factor calculations show that the T_N for $U = 4$ is smaller than the T_N for $U = 8$ [see Figs. 2(c) and (d)]. The T_N and the T_{MIT} of the bulk system are equal to each other for $U = 4$. On the other hand the T_{MIT} is much larger than T_N for $U = 8$. A paramagnetic insulating (PM-I) phase intervenes between the PM-M* and AF-I phase at larger U values. We also plot the specific heat C_v vs temperature for $U = 8$ case in Fig. 2(d). The high-temperature C_v peak associated with charge-fluctuations coincides with the T_{MIT} whereas the low-T peak of C_v associated with spin-fluctuations matches well with the T_N ^{82,83}. It is also apparent that, for $U = 4$, the local magnetic mo-

ment M in PM-M phase decreases upon decreasing the temperature from $T \sim 1$ up to T_N with the enhancement of the metallicity as shown in Fig. 2(b). Below T_N the local magnetic moment M increases again with decreasing the temperature. For $U = 8$ the magnetic moment M gradually increases with decreasing the temperature barring a small peak around T_N and saturates at low temperatures. The small drop just below T_N is due to the delocalization of the electrons assisted by virtual hopping facilitated by the antiferromagnetic correlations. The local moment for both $U = 4$ and $U = 8$ converge to the asymptotic value $M = 0.5$ at very high temperatures. So, the system directly transforms to an AF-I state from PM-M state upon cooling for $U < 8$ whereas the system switches to an AF-I from PM-M* via a PM-I state for larger U values as shown in our phase diagram. Overall, the bulk phase diagram obtained in our semi-classical Monte-Carlo (s-MC) approach is consistent with the DQMC^{84,85}, 2D cluster-DMFT (C-DMFT)⁸⁶, 3D cluster-DMFT (C-DMFT)⁸⁷ with vortex corrections and QMC simulations⁸⁸.

Next, we discuss the $U - T$ phase diagram for different AF/PM superlattices, namely 5/1, 3/1 and 1/1 SLs where $x \geq 0.5$ (x denotes fraction of correlated planes). We start our analysis with the 5/1 SL [see Fig. 3(a)]. The nonmonotonic behavior of T_N with U remains intact for 5/1 SL, similar to the bulk systems although the T_N values decrease very slightly. The T_{MIT} for $U < 8$ also coincides with the T_N (i.e. the SL system is metallic above the T_N) and the local magnetic moment decreases as we approach the T_N from the high temperature [see Fig. 3(c) for $U = 4$ case]. As a result the PM-M phase, observed in 5/1 SL, remains very similar to the bulk system. PM-M* phase is enlarged for intermediate U values as compared to the bulk phase diagram [please compare Fig. 3(a) and Fig. 2(a)]. To analyze the enlarged PM-M* phase further we compare the T_N and T_{MIT} obtained from the antiferromagnetic correlations and the resistivity curves, respectively in Fig. 3(b). Interestingly for $U = 8$ reduction in T_N is hardly noticeable. On the other hand the T_{MIT} decreases considerably due to the insertion of the uncorrelated layers. But, T_{MIT} still remains larger than the T_N . Magnetotransport properties of individual layers (comprised of $U = 8$ and $U = 0$) will be discussed later. In this PM-M* phase the magnetic moments in the correlated layer M_U gets more and more localized as we decrease the temperature (see $U = 8$ case in Fig. 3(c)) unlike the $U = 4$ case.

Now we outline the magnetotransport properties and the phase diagram of 3/1 SL. The T_N profile of 3/1 SL remains more or less the same to that of 5/1 SL (see Fig. 3(d)). We show the comparison of the T_N of 3/1 and 5/1 SLs in Fig. 3(b) for $U = 8$. Interestingly, the T_{MIT} coincides with the T_N at $U = 8$ in 3/1 SL (unlike 5/1 SL and the bulk systems) as shown in Fig. 3(b). In fact the T_N also coincides with T_{MIT} at larger U values. As a result the intervening PM-I phase seen between PM-M* and AF-I in 5/1 SL is overtaken by PM-M* phase.

So, one directly enters into an antiferromagnetic insulating (AF-I) phase from a paramagnetic metallic (PM-M*) phase in the 3/1 SL system with decrease in temperature. Similar phase diagram is also obtained for the 1/1 SL but the T_N [see the inset of Fig. 3(d)] gets reduced as compared to the 3/1 SL.

V. LONG RANGE ANTIFERROMAGNETIC ORDERING: MUTUAL COOPERATION BETWEEN CORRELATED AND UNCORRELATED LAYERS

In this section we analyze the magnetic and transport properties of the individual layers (i.e. separately for correlated ($U \neq 0$) and uncorrelated ($U = 0$) layers) of our SL systems to establish a mutual cooperation between the magnetic ordering of the correlated and uncorrelated layers. We plot the local moment M_U profile of the correlated layers for $U = 8$ and $U = 12$ for 5/1, 3/1 and 1/1 SLs in Fig. 4(a). The local moment M_U (calculated exclusively for correlated layers) gradually increases with decreasing the temperature for both the U values and saturates at low temperatures. The local moment in the correlated layer for 1/1 SL is visibly smaller than the 5/1 and 3/1 SLs below $T = 1$. The bidirectional coupling of the correlated plane with the adjacent uncorrelated planes in 1/1 SL suppresses the local moment in the correlated layers. As we increase the U values the local moment in the correlated layer for 1/1 SL approaches to that of the 3/1 and 5/1 SLs due to enhancement of the localization in the correlated layers. At low temperature $T = 0.02$, the local moment of the correlated layers increases monotonically with increase of U (since the double occupancy reduces with increase of U) and saturates at large U values as shown in Fig. 4(b). But, the local moment M_U in the correlated layer for 1/1 SL is smaller than the 3/1 and 5/1 SLs for intermediate U values as mentioned above. Otherwise, the qualitative nature of the local moments profile in the correlated layers remains similar for the 5/1, 3/1 and 1/1 SLs.

On the other hand, the average induced moment in the uncorrelated layer (M_0) shows nonmonotonic behavior with increase of U values and the maximum moment is obtained for $U = 8$ for all the three SLs [see Fig. 4(c)]. These induced moments in the uncorrelated layer are generated due to the kinetic hopping of the charge carriers from the correlated layers. In addition, it is apparently clear that the induced moment M_0 in uncorrelated layers for 1/1 SL is substantially smaller than the 3/1 and 5/1 superlattices. The induced magnetic moment in the uncorrelated layer is similar to the experimentally observed induced magnetic moment in the paramagnetic Pd layer in NiO/ Pd multilayers^{61–65} and the induced magnetic moment in Cu layer in CuO/ Cu multilayers⁶⁶.

In order to extract the temperature scale at which magnetic moments are actually induced in the uncorrelated layers we plot the local moment of uncorrelated layers vs

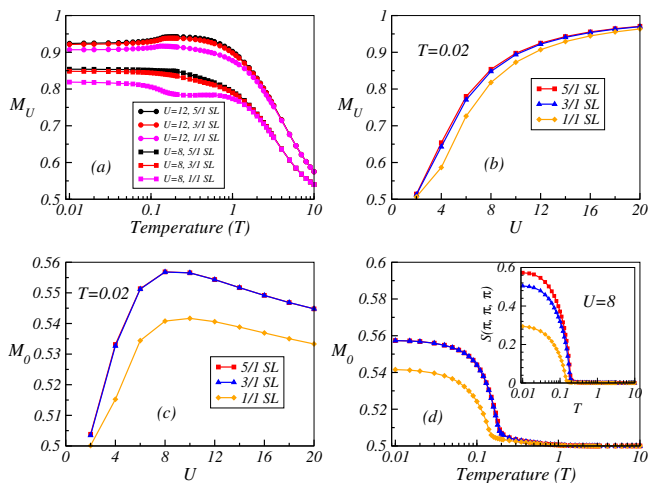


FIG. 4: (a) Temperature evolution of the local moments in the correlated layer (M_U) of three different superlattices (5/1, 3/1 and 1/1 SLs) are plotted for $U = 8$ and $U = 12$. The local moment increases monotonically with decreasing temperature and saturates at low temperature. For both values of U , the local moment in the 1/1 SL is smaller than the 3/1 and 5/1 SLs. (b) At low temperatures ($T = 0.02$), the local moment in the correlated layer (M_U) increases with U and eventually saturates for larger U values. The local moment M_U in 1/1 SL is smaller than the 3/1 and 5/1 SLs for intermediate U values. (c) The induced moment in the uncorrelated layer (M_0) for 5/1, 3/1 and 1/1 SLs exhibits a nonmonotonic behavior with U at low temperatures ($T = 0.02$). The induced moment in the 1/1 SL is considerably smaller than the 3/1 and 5/1 SLs. (d) For $U = 8$ the onset temperature of the induced moment in the uncorrelated layer (main panel) is consistent with the antiferromagnetic ordering temperature of the SL systems (inset).

temperature for 5/1, 3/1, and 1/1 SLs for $U = 8$ case in Fig. 4(d). Local moments are induced in the uncorrelated layer at very low temperatures (the temperature where M_0 becomes greater than 0.5) as compared to the correlated layers. The onset temperature of the induced moment in the uncorrelated layer (M_0) around $T = 0.2$ matches well with the T_N of these SL systems (see the inset of Fig. 4(d)). So our calculations show a one-to-one correspondence between antiferromagnetic ordering and onset of induced moments in uncorrelated layers in the SL systems.

To further analyze the correspondence between the onset of antiferromagnetic ordering in correlated and uncorrelated layers we plot $S(\pi, \pi, \pi)$ structure factor of both the layers separately and compare it with the $S(\pi, \pi, \pi)$ structure factor of the total SL system in Figs. 5(a)-(c). The structure factors show that the antiferromagnetic order appears at the same temperature for both correlated layers ($U \neq 0$ layers) and uncorrelated layers ($U = 0$ layers) and matches well with the T_N of the whole superlattice system. This also indicates that the correlations among the induced moments in the uncorrelated layer play an important role in mediating the long range in-

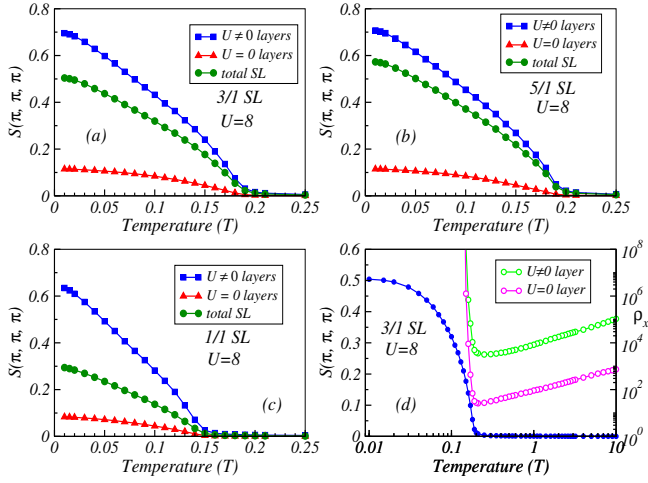


FIG. 5: Comparison of the antiferromagnetic ordering temperature (from $S(\pi, \pi, \pi)$ vs T plots) between the correlated layers ($U \neq 0$), uncorrelated layers ($U = 0$), and total SL (including both correlated and uncorrelated layers) for $U = 8$ in (a) 3/1 SL, (b) 5/1 SL, and (c) 1/1 SL. Individual correlated and uncorrelated layers exhibit antiferromagnetic transitions simultaneously which matches with T_N of whole SL system. A mutual cooperation between correlated and uncorrelated layers establishes the long range AF order in the whole superlattices. (d) In-plane resistivity ρ_x of the correlated and uncorrelated layers for 3/1 SL at $U = 8$ show that the MIT occurs at T_N . For a better clarity we have also re-plotted the temperature dependence of $S(\pi, \pi, \pi)$ for 3/1 SL in the same figure.

interactions between the correlated layers. So, overall the cooperation between the correlated and uncorrelated layers helps to sustain the global long range AF order in the superlattices. We also plot the layer resolved resistivities for the 3/1 SL in Fig. 5 (d). $S(\pi, \pi, \pi)$ of whole 3/1 SL is re-plotted in the same figure for comparing the transition temperatures. The T_{MIT} obtained from correlated layers and uncorrelated layers are equal to each other and coincides with the T_N for the SL system.

VI. PLANE RESOLVED TRANSPORT PROPERTIES OF THE SUPERLATTICES

Here, we investigate the plane resolved transport properties of the correlated and uncorrelated layers of the superlattices. First we focus on 3/1 SL where only one uncorrelated plane ($U = 0$) is intercalated between the correlated layers made up of three correlated planes. For this we evaluate the in-plane resistivity (ρ_x) of individual planes (three correlated planes and one uncorrelated plane) for $U = 8$ as shown in Fig. 6(a). Interestingly, the metal-insulator transition temperature of the edge correlated planes (T_{MIT}^E) is smaller than the center (T_{MIT}^C) correlated planes (i.e., $T_{MIT}^E < T_{MIT}^C$) in 3/1 SL. It is clearly observed that the center correlated plane exhibits MIT above T_N whereas the T_{MIT} of both the edge planes

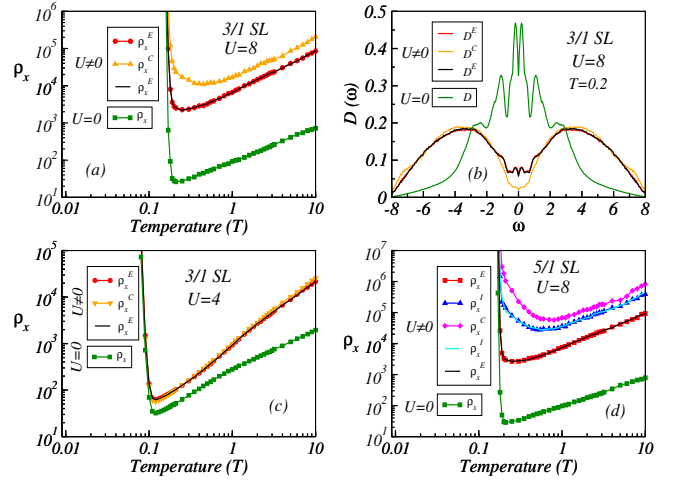


FIG. 6: In-plane resistivity (ρ_x) vs temperature (T) for all the constituent planes (three correlated planes and one uncorrelated plane) of the 3/1 SL are plotted for (a) $U = 8$ and (c) $U = 4$. For $U = 8$, both the T_{MIT} as well as the magnitude of the resistivity (ρ_x) of the edge correlated planes are smaller than that of the center correlated plane (i.e. $T_{MIT}^E < T_{MIT}^C$ and $\rho_x^E < \rho_x^C$). The T_{MIT} of the edge correlated plane matches with T_N . In case of $U = 4$ all the individual planes show MIT exactly at T_N . In fact, for $U = 4$, the resistivity curves obtained from the correlated planes are overlapping on top of each other. The resistivity of the uncorrelated plane ($U = 0$) is much smaller than the correlated planes for both U values. (b) Plane resolved density of states (DOS) of the 3/1 SL at $T = 0.2$ (around T_N): The weight of the DOS at the Fermi level ($\omega = 0$) for the edge correlated planes are larger than the central correlated plane ($D^E > D^C$). But, the weight of the DOS of the uncorrelated plane ($U = 0$) at the Fermi level is very predominant among the four planes. Our plane resolved DOS calculations correspond well with the in-plane resistivity calculations shown in (a). (d) In-plane resistivity of the individual planes in 5/1 SL at $U = 8$ shows similar characteristics behavior to that of 3/1 SL in (a). Both the T_{MIT} and magnitude of ρ_x increase as we move from the edge plane to the center plane inside the correlated layer. Also the ρ_x in the uncorrelated plane ($U = 0$) is much smaller than the correlated planes. Here E, I, and C stand for edge, intermediate and center planes, respectively.

coincides with the T_N . The T_{MIT} of the uncorrelated plane also matches with the T_N . Expectedly the value of ρ_x in the uncorrelated plane is much smaller than the correlated plane.

Next, we calculate plane-resolved density of states (DOS) to further deliberate the transport properties. Plane-resolved DOS of the correlated layer at $T = 0.2$ (see Fig. 6(b)) indicate that weight of the DOS of the edge correlated planes at the Fermi level (set at $\omega = \epsilon_F = 0$) are larger as compared to the central correlated plane (i.e. $D^E > D^C$ at $\omega = 0$). Expectedly the weight of DOS of the uncorrelated plane at Fermi level is significantly greater than all the correlated planes. Hence, our plane-resolved DOS calculations are coherent with the in-plane resistivity calculations of the individual planes

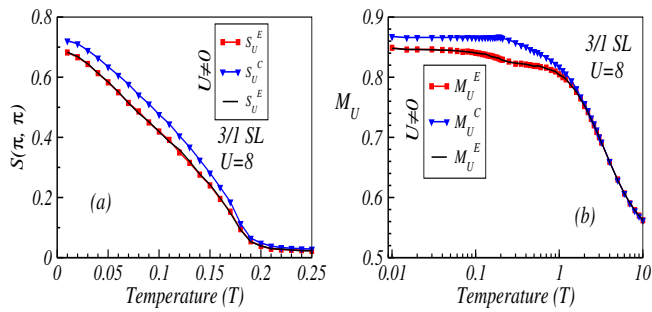


FIG. 7: (a) Temperature dependence of $S(\pi, \pi)$ of the individual correlated planes ($U \neq 0$) of 3/1 SL at $U = 8$ are plotted to compare the T_{NS} . Antiferromagnetic transition temperatures remain more or less same for the individual constituent planes (two edge planes and one center plane). $S(\pi, \pi)$ of the edge plane is smaller than the center plane at low temperatures. (b) The local moments in the edge correlated planes of the 3/1 SL are smaller than the center correlated plane ($M_U^E < M_U^C$) at low temperatures corresponds well with the structure factor calculations presented in (a).

of the superlattice.

For smaller U values all the planes (comprised of three correlated planes and one uncorrelated plane) show metal-insulator transition at the same temperature [see Fig. 6(c)] and this temperature coincides with the T_N . In fact, the resistivity curves of all three correlated planes overlap with each other. This shows that all the correlated planes are equally affected by the insertion of uncorrelated layer for smaller U values where moments are much more delocalized as compared to higher U values. Our magnetotransport results qualitatively follow the QMC⁶⁷ and DQMC⁶⁹ studies of the correlated superlattices where it was shown that the correlated layer is affected by the uncorrelated layer and the effect increases with decrease of U . But, the detailed transport properties were not reported earlier. The transport properties of 5/1 SL [see Fig. 6(d)] remains qualitatively similar to that of 3/1 SL where the T_{MIT} increases as we move from the edge plane to the center plane.

In our 3/1 SL the correlated layer is made up of three planes. So the obvious question arises at this point: Does all the three correlated planes (two edge planes and one center plane) that constitute the correlated layer align antiferromagnetically at the same temperature or not? To answer this question we plot the antiferromagnetic structure factor of all the three correlated planes separately using $U = 8$ in Fig. 7(a). The AF correlations of individual planes vanish at the same temperature. But, the reduction in the low-temperature saturation value in edge plane as compared to center plane is very clear. This may be due to the larger magnetic moment in the center plane than the edge planes. To confirm this we plot the local magnetic moment M_U of individual correlated planes vs temperature in Fig. 7(b). In fact, the M_U for the center plane is larger than the edge plane at low temperatures.

The uncorrelated plane affects the local magnetic mo-

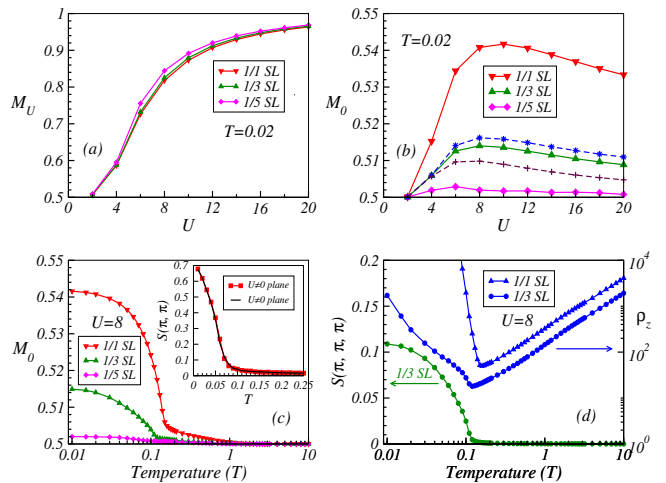


FIG. 8: Magnetotransport properties of 1/3, and 1/5 SLs. We re-plot the corresponding data of 1/1 SL for comparison. (a) At low temperatures ($T = 0.02$) the local moment in the correlated layer increases monotonically with U and saturates at higher values of U for both 1/3 and 1/5 SLs similar to 1/1 SL. (b) The induced moment in the uncorrelated layer at $T = 0.02$ shows nonmonotonic behavior with U for 1/3 SL. However, for the 1/5 SL, the induced moment in the uncorrelated layer is negligibly small for all values of U . Induced moment profile of the edge (center) uncorrelated plane for 1/3 SL is also plotted by blue (maroon) dashed line. Expectedly, induced moment in the edge plane is larger than the center plane. (c) Temperature dependence of M_0 for $U = 8$ show that there is a clear onset temperature of the induced moment in the uncorrelated layer in 1/3 SLs, similar to 1/1 SL. There is no clear onset temperature for 1/5 SL. In the inset, temperature dependence of the structure factor $S(\pi, \pi)$ for the correlated planes separated by five uncorrelated planes in 1/5 SL are plotted for $U = 8$. Individual correlated planes show antiferromagnetic transitions, but the long range antiferromagnetic order between them is not feasible due to the insufficient induced moment in the uncorrelated layer, which acts as a mediator. (d) Temperature dependence of $S(\pi, \pi)$ for 1/3 SL at $U = 8$ (left axis) shows a clear antiferromagnetic transition. The T_{MIT} obtained from ρ_z vs T plot matches well with the T_N for 1/3 SL. The value of ρ_z in 1/3 SL is smaller than the 1/1 SL due to the insertion of a thicker uncorrelated layer between the correlated layers.

ments M_U of the correlated planes differently (M_U is larger for central plane) due to the proximity effect as we discussed earlier. Apparently the M_U profiles indicate that the resulting effective U (U_{eff}) of center plane is larger than the edge plane. This is also supported from resistivity plots where T_{MIT} of the center plane is larger than the edge plane (see Fig. 6 (a)). From all these analysis one would naively expect that the T_N of the edge plane should be smaller than the center plane but this difference is beyond the resolution of our calculations and we get more or less same T_N [see Fig. 7(a)].

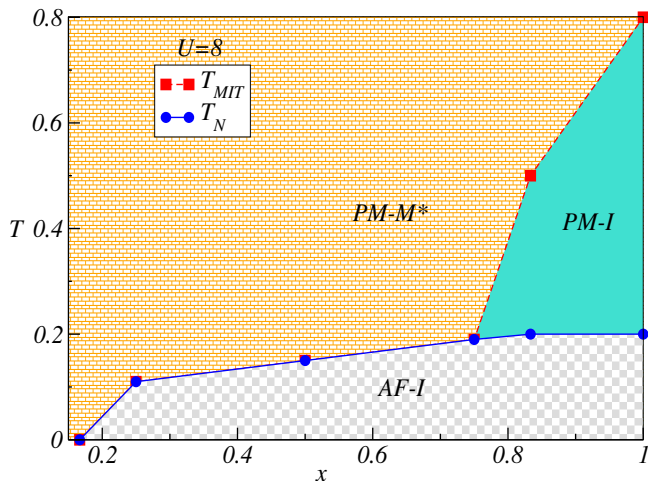


FIG. 9: $x-T$ phase diagram comprises different superlattices (where $w_U = 1$ or/and $w_0 = 1$) for $U = 8$. Here, $x = \frac{w_U}{w_U + w_0}$ is the fraction of correlated planes ($U \neq 0$). $x = 1$ represents the bulk system where all the sites have $U \neq 0$. We use the results from 1/5 SL ($x \sim 0.17$), 1/3 SL ($x \sim 0.25$), 1/1 SL ($x \sim 0.5$), 3/1 SL ($x \sim 0.75$), 5/1 SL ($x \sim 0.83$) and bulk ($x \sim 1$) to plot the phase diagram. Both T_N (blue line) and T_{MIT} (red dashed line) decrease as we decrease the x value. System encounters a PM-I phase between the AF-I and PM-M* phases for $x > 0.75$. The T_{MIT} merges with the T_N for $x \leq 0.75$ i.e. the system directly transits from PM-M* to AF-I state upon cooling. At $x \sim 0.17$ (for 1/5 SL) the long range AF order collapses due to the insufficient induced moments in the uncorrelated layers as discussed earlier in Fig. 8(c).

VII. MAGNETOTRANSPORT PROPERTIES OF 1/3 AND 1/5 SUPERLATTICES

Now we briefly analyze the transport and magnetic properties of 1/3 and 1/5 SLs to present a $x-T$ diagram. We plot the local moment of the correlated layers for 1/1, 1/3 and 1/5 SLs with different U values at $T = 0.02$. The local moments of the correlated layers M_U increases monotonically with increase of U and saturates at large U values as shown in Fig. 8(a) for all three SLs. So, the qualitative nature of the local moments profile in the correlated planes remains the same as we increase the thickness of uncorrelated layer. We also plot the induced magnetic moment in uncorrelated layers in Fig. 8(b). Induced magnetic moment shows nonmonotonic behavior for 1/1 and 1/3 SLs. But, induced magnetic moment decreases drastically for 1/5 SL. The average induced moment M_0 in the edge and center uncorrelated ($U = 0$) planes are also plotted (see Fig. 8(b)) for 1/3 SL. The nonmonotonic behavior remains intact for both edge and center plane and expectedly the induced moment in the edge uncorrelated plane is larger than the center uncorrelated plane.

The induced moments in the uncorrelated layer decreases as we shift from 1/1 to 1/3 SL as shown in Fig. 8(b). But, there is a clear onset temperature of the

induced moment in the uncorrelated layer (M_0) around $T = 0.1$ for 1/3 SL as shown in Fig. 8(c). So, one expect long range antiferromagnetic correlations in 1/3 SL. In fact, magnetic structure factor $S(\pi, \pi, \pi)$ for 1/3 SL (see Fig. 8(d)) shows that the SL system is antiferromagnetic at low temperatures. Resistivity curve, plotted in same figure, shows that the T_{MIT} matches well with the T_N . Expectedly the resistivity of 1/3 SL is much lower than the 1/1 SL due to participations of thicker uncorrelated layer (see Fig. 8(d)).

Does the 1/5 SL system have an antiferromagnetic ordering at low temperatures? Our calculations show that the induced moment in uncorrelated layers for 1/5 SL is negligible (see Fig. 8 (b) and (c)) and as result the long range antiferromagnetic correlation between the correlated layers cease to exist. To gain more insight of magnetic correlations of correlated planes separated by five uncorrelated planes we plot the magnetic structure factor $S(\pi, \pi)$ for individual correlated planes in the inset of Fig. 8(c). It is apparent that the individual correlated layers are antiferromagnetically ordered by themselves but due to insufficient induced moments in uncorrelated planes the long range antiferromagnetic order between them is not established.

VIII. $x-T$ PHASE DIAGRAM

Thereafter, we present the $x-T$ phase diagram for the correlated/uncorrelated SLs for $U = 8$ where $w_U = 1$ or/and $w_0 = 1$. The Neel temperature T_N [from $S(\pi, \pi, \pi) - T$ plots] and the metal-insulator transition temperature T_{MIT} [from $\rho_z - T$ plot] for different SLs are used to construct this phase diagram. Fraction of correlated planes x is varied in our SLs. We plot the T_N for 1/5 SL ($x \sim 0.17$), 1/3 SL ($x \sim 0.25$), 1/1 SL ($x \sim 0.5$), 3/1 SL ($x \sim 0.75$), 5/1 SL ($x \sim 0.83$) and bulk ($x \sim 1$) in Fig. 9. For bulk case ($x = 1$) the system transits from PM-I phase to an AF-I phase as we discussed earlier. This PM-I to AF-I transition remains intact for 5/1 SL ($x \sim 0.83$) although the T_{MIT} decreases considerably. For $x \leq 0.75$ the PM-I phase above AF-I phase disappears and as a result the T_{MIT} matches well with the T_N . Lastly, the antiferromagnetic ordering vanishes for 1/5 SL (i.e. for $x \sim 0.17$). So, to summarize, the superlattice system directly transits from AF-I state to PM-M* state with increase of temperature for $x \leq 0.75$ whereas the SL system converts to PM-M* state from AF-I state via the PM-I state upon increasing the temperature for $x > 0.75$ at $U = 8$. This phase diagram is similar to the very recently reported phase diagram in Ref. 72, where randomly diluted systems were studied.

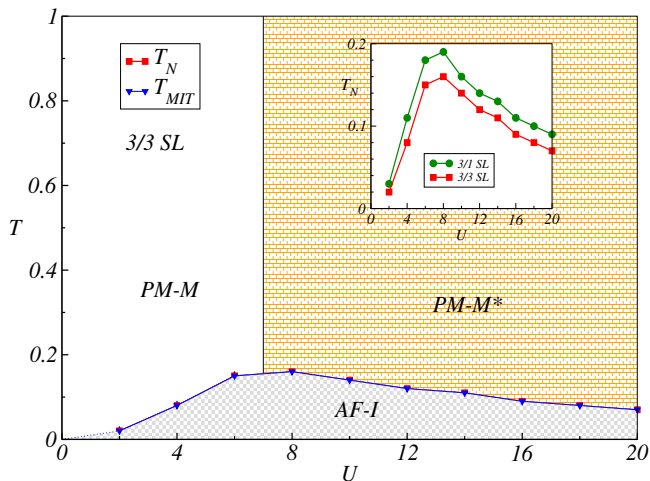


FIG. 10: $U - T$ phase diagram of the 3/3 superlattice. The phase diagram is very similar to the phase diagram for 3/1 SL in Fig. 3(d). The only difference is that the value of T_N is suppressed. We compare the T_N values in the inset.

IX. MAGNETOTRANSPORT PROPERTIES OF 3/3 SL

Now we proceed to study the plane resolved magnetic and transport properties for 3/3 SL ($x = 0.5$). First, we plot the $U - T$ phase diagram for 3/3 SL in Fig. 10. This phase diagram is very similar to 3/1 and 1/1 SLs that we presented in Fig. 3(d). We plot the antiferromagnetic structure factor and resistivities (ρ_x and ρ_z) for the 3/3 SL in Fig. 11(a) for $U = 8$. The T_N of 3/3 SL remains more or less same to that of 1/1 SL. The T_{MIT} obtained from ρ_z and ρ_x are also equal to each other and matches well with the T_N . Obviously, the value of out-of-plane resistivity ρ_z is larger than in-plane resistivity ρ_x . The plane resolved resistivities of the correlated and uncorrelated layers are shown in Fig. 11(b). The T_{MIT} of central correlated plane is larger than the edge correlated planes. Interestingly, only the T_{MIT} of the edge correlated plane matches with the T_N . On the other hand, all the uncorrelated planes show the metal-insulator transition at T_N . In addition it is clear that the central correlated (uncorrelated) plane is more (less) resistive than the edge correlated (uncorrelated) planes in correlated (uncorrelated) layer. The coupling of the correlated edge plane with the nearest uncorrelated plane reduces its resistivity as compared to the central correlated plane. In other words metallicity penetrates to the correlated edge layer above the T_N due to the interfacial coupling between the correlated and uncorrelated layers. This interfacial coupling is also reflected in the plane resolved magnetic moments profile of the correlated layer shown in Fig. 11(c). We find that the center plane has larger moment as compared to the edge planes at low temperatures. Expectedly the edge plane of the uncorrelated layer also has comparatively larger induced magnetic moment to that of center plane as shown in the same figure.

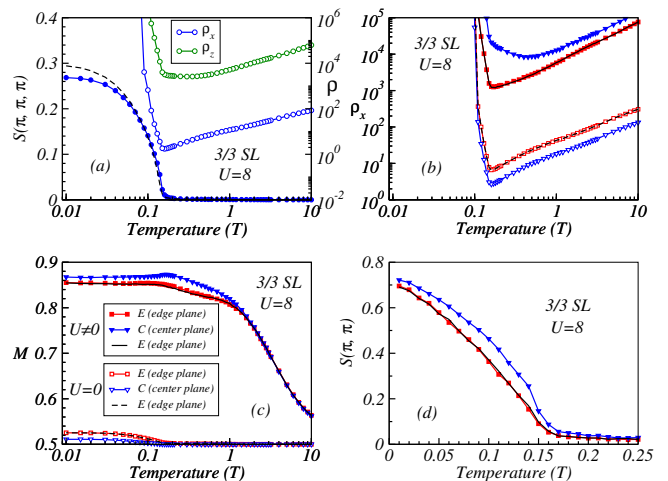


FIG. 11: (a) Temperature evolution of the structure factor (left axis) and out-of-plane ρ_z and in-plane ρ_x resistivities (right axis) are plotted for 3/3 SL for $U = 8$. It is apparent that the T_{MIT} s obtained from ρ_x and ρ_z are equal to each other and matches well with the T_N of the SL. The structure factor of 1/1 SL is plotted by dashed line to compare the T_N s. The magnitude of ρ_z is much larger than ρ_x , as expected. (b) The in-plane resistivity ρ_x of the constituent planes of the correlated ($U \neq 0$) and uncorrelated ($U = 0$) layers: The T_{MIT} and the value of ρ_x in the central correlated plane are larger than that of the edge correlated planes (i.e. $T_{MIT}^E < T_{MIT}^C$ and $\rho_x^E < \rho_x^C$). Edge correlated planes show MIT exactly at T_N . All the uncorrelated planes also show MIT at the same temperature $T = T_N$. But, the value of ρ_x in the edge uncorrelated plane is somewhat larger than the center uncorrelated plane ($\rho_x^E > \rho_x^C$). The local moment profile of all the individual planes are presented in (c). In the correlated layer, the local moments in the edge plane M_U^E is smaller than the center plane M_U^C (i.e. $M_U^E < M_U^C$) at low temperatures. Conversely, in the uncorrelated layer, the induced moments in the edge plane M_0^E is larger than the center plane M_0^C (i.e. $M_0^E > M_0^C$). (d) Center correlated plane shows antiferromagnetic transition at slightly higher temperature than that of the edge correlated planes. The value of structure factor in the center plane is also larger than the edge planes ($S_U^E < S_U^C$) at low temperatures. This is consistent with the moment profile curves shown in (c). Legends are same in (b), (c), and (d). Physical observables like moment profile, resistivity and structure factors are symmetric around the central plane in both correlated and uncorrelated layers.

Now, the same question that we addressed for 3/1 SL arises here: Does all the three correlated planes (two edge planes and one center plane) that constitute the correlated layer in the 3/3 SL align antiferromagnetically at the same temperature? To answer this question we plot the antiferromagnetic structure factor of the three correlated planes for $U = 8$ in Fig. 11(d). The T_N of the center plane is slightly higher than the edge planes which is expected. So, one can firmly claim that the effective U (U_{eff}) of the central plane is somewhat larger than the edge planes.

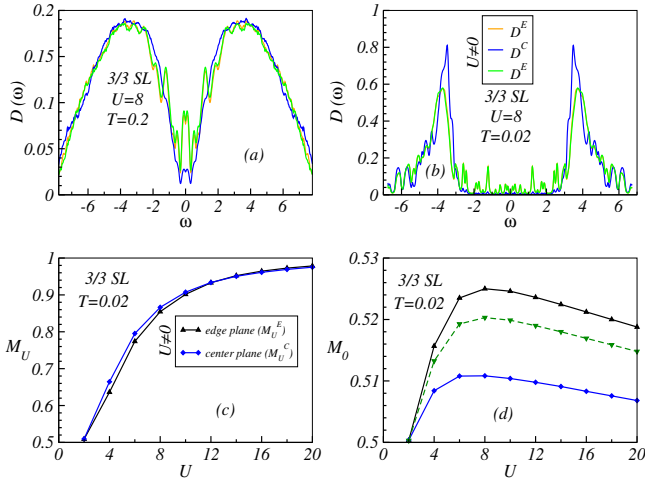


FIG. 12: The density of states (DOS) of the constituent planes of the correlated layer ($U \neq 0$) in the 3/3 SL are plotted for $U = 8$ at (a) $T = 0.2$ (around T_N) and (b) $T = 0.02$ (low temperatures). Mott lobes appear around $\omega = \pm \frac{U}{2}$. At high temperatures $T = 0.2$ the weight of DOS of the edge correlated plane at the Fermi level ($\omega = 0$) is greater than that of the center correlated plane ($D^E > D^C$), supporting the in-plane resistivity calculations shown in Fig. 11(b). A clear Mott gap opens up in both the center and edge planes of correlated layer at low temperatures $T = 0.02$. But, extra tiny satellite pattern arises in the band-gap of the edge plane. (c) At low temperatures ($T = 0.02$), the local moment in both the edge and center planes of the correlated layer increase monotonically with increase of U and saturates at higher U values. The local moment in the edge plane is smaller than the center plane ($M_U^E < M_U^C$) for intermediate values of U . (d) The U dependence of the induced moment in the edge and center uncorrelated planes at low temperatures $T = 0.02$ exhibits nonmonotonic behavior (optimum value around $U = 8$). The induced moment in the edge uncorrelated plane is larger than the center uncorrelated plane ($M_0^E > M_0^C$). The average induced moment profile is plotted by dashed line for comparison. Legends are same in (c) and (d).

To analyze the plane resolved magnetic and transport properties further we have calculated the density of states (DOS) of the individual correlated planes of the 3/3 SL. The DOS ($D(\omega)$) of the individual planes of the correlated layer are shown in Fig. 12(a) for $U = 8$ at temperature $T = 0.2$ (just above T_N). Emergence of Mott lobes at $\omega = \pm \frac{U}{2}$ is apparent in all the three correlated planes. But the weight of DOS at the Fermi level ($\omega = 0$) for the edge correlated plane is comparatively larger than to that of the central correlated plane. This larger weight at the Fermi level enforces the edge correlated planes to have smaller resistivity than the center correlated plane. At low temperature $T = 0.02$ a clear Mott gap opens in the DOS of center correlated plane as shown in Fig. 12(b). Although same kind of gap is noticed for both the edge plane and center plane, some very tiny satellite patterned structures appear in the band-gap of edge planes.

At low temperatures ($T = 0.02$) the local moment of

the correlated planes increases monotonically with increase of U and saturates at large U values as shown in Fig. 12(c). The local moments in the center plane is slightly larger than the edge plane for intermediate U values. Otherwise, the qualitative monotonic nature of the local moments profile in the correlated planes remains the same. On the other hand the induced magnetic moment in uncorrelated layer shows nonmonotonic behavior (for both edge and center plane) with U at low temperatures. The induced local moment in the edge uncorrelated plane is significantly larger than the center uncorrelated plane as shown in Fig. 12(d). This is due to the fact that the uncorrelated edge plane which is adjacent to the correlated plane gets more affected by the correlated layer.

X. CONCLUSIONS

In this paper we have implemented one band Hubbard model at half-filling to investigate the AF/PM superlattices by using semi-classical Monte Carlo approach. We analyze various superlattices in three dimensions where correlated (with on-site repulsion strength $U \neq 0$) and uncorrelated ($U = 0$) layers are arranged periodically. First, we explore the $U - T$ phase diagrams for various $wU/1$ SLs ($wU = 5, 3, 1$) and compare the results with the bulk systems. We show that the magnetic moments are induced in the uncorrelated layers at low temperatures due to the kinetic hopping of carriers and optimum magnetic moment is induced for $U = 8$. The antiferromagnetic ordering among the induced moments in uncorrelated layers mediates the long range antiferromagnetic ordering between the correlated layers and as a result the antiferromagnetic insulating nature of the bulk systems remains intact in the SLs. In other words, the long range antiferromagnetic order survives in the superlattices through the mutual cooperation of the induced moment in the uncorrelated layer and the local moment in the correlated layer. Thus, the induced moments in the uncorrelated layer play an important role in determining the global long range antiferromagnetic order in the superlattices.

To analyze the plane resolved magnetotransport properties we focus on the $U = 8$ regime. Interestingly, the average local moments in the edge planes are comparatively smaller than the central plane in the correlated layer. The coupling of the edge planes of correlated and uncorrelated layers reduces the local magnetic moments of the edge correlated plane but induces magnetic moments in uncorrelated layer. In-plane resistivity calculations of the individual constituent planes of the superlattices show that the T_{MIT} increases as we move from edge plane to center plane inside the correlated layers, which is consistent with the local moment profile of the individual constituent planes. So overall our plane resolved calculations establish an one-to-one connection between the local moment profile and the in-plane transport properties of the superlattices. Plane-resolved den-

sity of states calculations of the individual planes of the correlated layer are also concomitant with the in-plane resistivities. On the other hand the induced moments in uncorrelated planes decreases considerably as a function of the distance from the interface, but the metal-insulator transition temperature of edge and center planes remain more or less unaffected. In the end, we show that the induced moments in uncorrelated layers dissipates with

increasing the thickness of uncorrelated layers as a result the antiferromagnetic ordering among correlated layers vanishes.

ACKNOWLEDGMENT

We acknowledge use of the Meghnad2019 computer cluster at SINP.

-
- ¹ H. Y. Hwang, Y. Iwasa, M. Kawasaki, B. Keimer, N. Nagaosa, and Y. Tokura, *Nat. Mater.* **11**, 103 (2012).
 - ² J. Chakhalian, A. J. Millis, and J. Rondinelli, *Nat. Mater.* **11**, 92 (2012).
 - ³ J. Chakhalian, J. W. Freeland, A. J. Millis, C. Panagopoulos, and J. M. Rondinelli, *Rev. Mod. Phys.* **86**, 1189 (2014).
 - ⁴ A. Bhattacharya and S. J. May, *Annu. Rev. Mater. Res.* **44**, 65 (2014).
 - ⁵ P. Zubko, S. Gariglio, M. Gabay, P. Ghosez, and J. M. Triscone, *Annu. Rev. Condens. Matter Phys.* **2**, 141 (2011).
 - ⁶ D. G. Schlom, D. G., L.-Q. Chen, X. Pan, A. Schmehl, and M. A. Zurbuchen, *J. Am. Ceram. Soc.* **91**, 2429 (2008).
 - ⁷ S. Middey, J. Chakhalian, P. Mahadevan, J.W. Freeland, A.J. Millis, and D.D. Sarma, *Annu. Rev. Mater. Res.* **46**, 305 (2016).
 - ⁸ J. Stahn, J. Chakhalian, C. Niedermayer, J. Hoppler, T. Gutberlet, J. Voigt, F. Treubel, H.-U. Habermeier, G. Cristiani, B. Keimer, and C. Bernhard, *Phys. Rev. B* **71**, 140509(R) (2005).
 - ⁹ J. Chakhalian, J. W. Freeland, G. Srajer, J. Stempffer, G. Khaliullin, J. C. Cezar, T. Charlton, R. Dalgliesh, C. Bernhard, G. Cristian, H. -U. Habermeier, and B. Keimer, *Nat. Phys.* **2**, 244 (2006).
 - ¹⁰ K. S. Takahashi, M. Kawasaki, Y. Tokura, *Appl. Phys. Lett.* **79**, 1324 (2001).
 - ¹¹ A. V. Boris, Y. Matiks, E. Benckiser, A. Frano, P. Popovich, V. Hinkov, P. Wochner, M. Castro-Colin, E. Demple, V. K. Malik, C. Bernhard, T. Prokscha, A. Suter, Z. Salman, E. Morenzoni, G. Cristiani, H. -U. Habermeier, B. Keimer, *Science* **332**, 937 (2011).
 - ¹² S. Okamoto, and A. Millis, *Nature* **428**, 630 (2004).
 - ¹³ S. Okamoto, *Phys. Rev. B* **82**, 024427 (2010).
 - ¹⁴ Y. Cao, Xiaoran Liu, M. Kareev, D. Choudhury, S. Middey, D. Meyers, J. -W. Kim, P. J. Ryan, J. W. Freeland, and J. Chakhalian, *Nat. Commun.* **7**, 10418 (2016).
 - ¹⁵ X. R. Wang, C. J. Li, W. M. Lü, T. R. Paudel, D. P. Leusink, M. Hoek, N. Poccia, A. Vailionis, T. Venkatesan, J. M. D. Coey, E. Y. Tsymbal, Ariando, and H. Hilgenkamp, *Science* **349**, 716 (2015).
 - ¹⁶ F. Y. Bruno, J. Garcia-Barriocanal, M. Varela, N. M. Nemes, P. Thakur, J. C. Cezar, N. B. Brookes, A. Rivera-Calzada, M. Garcia-Hernandez, C. Leon, S. Okamoto, S. J. Pennycook, and J. Santamaria, *Phys. Rev. Lett.* **106**, 147205 (2011).
 - ¹⁷ J. S. Lee, D. A. Arena, P. Yu, C. S. Nelson, R. Fan, C. J. Kinane, S. Langridge, M. D. Rossell, R. Ramesh, and C. C. Kao, *Phys. Rev. Lett.* **105**, 257204 (2010).
 - ¹⁸ A. Tebano, A. Orsini, P. G. Medaglia, D. DiCastro, G. Balestrino, B. Freelon, A. Bostwick, Y. J. Chang, G. Gaines, E. Rotenberg, and N. L. Saini, *Phys. Rev. B* **82**, 214407 (2010).
 - ¹⁹ A. Tebano, C. Aruta, S. Sanna, P. G. Medaglia, G. Balestrino, A. A. Sidorenko, R. DeRenzi, G. Ghiringhelli, L. Braicovich, V. Bisogni, and N. B. Brookes, *Phys. Rev. Lett.* **100**, 137401 (2008).
 - ²⁰ J. Chakhalian, J. W. Freeland, H.-U. Habermeier, G. Cristiani, G. Khaliullin, M. van Veenendaal, B. Keimer Chakhalian, *Science* **318**, 1114 (2007).
 - ²¹ J. J. Peng, C. Song, F. Li, B. Cui, H. J. Mao, Y. Y. Wang, G. Y. Wang, F. Pan, *ACS Appl. Mater. Interfaces* **7**, 17700 (2015).
 - ²² J. Liu, S. Okamoto, M. van Veenendaal, M. Kareev, B. Gray, P. Ryan, J. W. Freeland, and J. Chakhalian, *Phys. Rev. B* **83**, 161102 (2011).
 - ²³ J. Liu, M. Kareev, D. Meyers, B. Gray, P. Ryan, J. W. Freeland, and J. Chakhalian, *Phys. Rev. Lett.* **109**, 107402 (2012).
 - ²⁴ H. Chen, D. P. Kumah, A. S. Disa, F. J. Walker, C. H. Ahn, and S. Ismail-Beigi, *Phys. Rev. Lett.* **110**, 186402 (2013).
 - ²⁵ M. C. Dekker, A. Herklotz, L. Schultz, M. Reibold, K. Vogel, M. D. Biegalski, H. M. Christen, and K. Dorr, *Phys. Rev. B* **84**, 054463 (2011).
 - ²⁶ H. Boschker, J. Kautz, E. P. Houwman, W. Siemons, D. H. A. Blank, M. Huijben, G. Koster, A. Vailionis, and G. Rijnders, *Phys. Rev. Lett.* **109**, 157207 (2012).
 - ²⁷ X. Li, I. L. Vrejoiu, M. Ziese, A. Gloter, and P. A. van Aken, *Scientific Reports* **7**, 40068 (2017).
 - ²⁸ S. J. May, P. J. Ryan, J. L. Robertson, J. -W. Kim, T. S. Santos, E. Karapetrova, J. L. Zarestky, X. Zhai, S. G. E. te Velthuis, J. N. Eckstein, S. D. Bader, and A. Bhattacharya, *Nat. Mater.* **8**, 892 (2009).
 - ²⁹ Q. H. Qin, L. Äkäsloppolo, N. Tuomisto, L. Yao, S. Majumdar, J. Vijayakumar, A. Casiraghi, S. Inkinen, B. Chen, A. Zugarramurdi, M. Puska, and S. van Dijken, *Adv. Mater.* **28**, 6852 (2016).
 - ³⁰ M. N. Grisolia, J. Varignon, G. Sanchez-Santolino, A. Arora, S. Valencia, M. Varela, R. Abrudan, E. Weschke, E. Schierle, J. E. Rault, J. -P. Rueff, A. Barthélémy, J. Santamaria and M. Bibes, *Nat. Phys.* **12**, 484 (2016).
 - ³¹ A. Ohtomo, H. Y. Hwang, *Nature* **427**, 423 (2004).
 - ³² A. Brinkman, M. Huijben, M. V. Zalk, J. Huijben, U. Zeitler, J. C. Maan, W. G. V. der Wiel, G. Rijnders, D. H. A. Blank, and H. Hilgenkamp, *Nat. Mater.* **6**, 493 (2007).
 - ³³ N. Reyren, S. Thiel, A. D. Caviglia, L. Fitting-Kourkoutis, G. Hammerl, C. Richter, C. W. Schneider, T. Kopp, A. S. Ruetschi, D. Jaccard, M. Gabay, D. A. Muller, J. M. Triscone, and J. Mannhart, *Science* **317**, 1196 (2007).
 - ³⁴ A. Ohtomo, D. A. Muller, J. L. Grazul, H. Hwang, *Nature* **419**, 378 (2002).
 - ³⁵ J. Zheng, W. Shi, Z. Li, J. Zhang, C. -Y. Yang, Z. Zhu, M.

- Wang, J. Zhang, F. Han, H. Zhang, Y. Chen, F. Hu, B. Shen, Y. Chen, and J. Sun, *ACS Nano* **18**, 9232 (2024).
- ³⁶ Y. Takamura, F. Yang, N. Kemik, E. Arenholz, M. D. Biegalski, and H. M. Christen, *Phys. Rev. B* **80**, 180417(R) (2009).
- ³⁷ J. D. Hoffman, B. J. Kirby, J. Kwon, Gilberto Fabbris, D. Meyers, J. W. Freeland, I. Martin, O. G. Heinonen, P. Steadman, H. Zhou, C. M. Schlepütz, M. P. M. Dean, S. G. E. te Velthuis, J. -M. Zuo, and A. Bhattacharya, *Phys. Rev. X* **6**, 041038 (2016).
- ³⁸ J. Garcia-Barriocanal, J. C. Cezar, F. Y. Bruno, P. Thakur, N. B. Brookes, C. Utfeld, A. Rivera-Calzada, S. R. Giblin, J. W. Taylor, J. A. Duffy, S. B. Dugdale, T. Nakamura, K. Kodama, C. Leon, S. Okamoto, and J. Santamaria, *Nat. Commun.* **1**, 82 (2010).
- ³⁹ N. Nakagawa, H. Y. Hwang, D. A. Muller, *Nat. Mater.* **5**, 204 (2006).
- ⁴⁰ T. Koida, M. Lippmaa, T. Fukumura, K. Itaka, Y. Matsumoto, M. Kawasaki, and H. Koinuma, *Phys. Rev. B* **66**, 144418 (2002).
- ⁴¹ A. Gozar, G. Logvenov, L. Fitting Kourkoutis, A. T. Bollinger, L. A. Giannuzzi, D. A. Muller, I. Bozovic, *Nature* **455**, 782 (2008).
- ⁴² D. A. Dikin, M. Mehta, C. W. Bark, C. M. Folkman, C. B. Eom, and V. Chandrasekhar, *Phys. Rev. Lett.* **107**, 056802 (2011).
- ⁴³ L. Li, C. Richter, J. Mannhart, and R. C. Ashoori, *Nat. Phys.* **7**, 762 (2011).
- ⁴⁴ J. A. Bert, B. Kalisky, C. Bell, M. Kim, Y. Hikita, H. Y. Hwang, and K. A. Moler, *Nat. Phys.* **7**, 767 (2011).
- ⁴⁵ S. S. A. Seo, W. S. Choi, H. N. Lee, L. Yu, K. W. Kim, C. Bernhard, T. W. Noh, *Phys. Rev. Lett.* **99**, 266801 (2007).
- ⁴⁶ G. Zhou, C. Song, Y. Bai, Z. Quan, F. Jiang, W. Liu, Y. Xu, S. S. Dhesi, X. Xu, *ACS Appl. Mater. Interfaces* **9**, 3156 (2017).
- ⁴⁷ M. Gibert, P. Zubko, R. Scherwitzl, J. niguez, J. -M. Triscone, *Nat. Mater.* **11**, 195 (2012).
- ⁴⁸ M. Gibert, M. Viret, A. Torres-Pardo, C. Piamonteze, P. Zubko, N. Jaouen, J. -M. Tonnerre, A. Mougin, J. Fowlie, S. Catalano, A. Gloter, O. Stephan, and J. -M. Triscone, *Nano Lett.* **15**, 7355 (2015).
- ⁴⁹ A. T. Lee, M. J. Han, *Phys. Rev. B* **88**, 035126 (2013).
- ⁵⁰ S. Dong, E. Dagotto, *Phys. Rev. B* **87**, 195116 (2013).
- ⁵¹ J. Hoffman, I. C. Tung, B. B. Nelson-Cheeseman, M. Liu, J. W. Freeland, A. Bhattacharya, *Phys. Rev. B* **88**, 144411 (2013).
- ⁵² C. Piamonteze, M. Gibert, J. Heirdler, S. Rusponi, H. Brune, H. -M. Triscone, F. Nolting, U. Staub, *Phys. Rev. B* **92**, 014426 (2015).
- ⁵³ A. J. Grutter, H. Yang, B. J. Kirby, M. R. Fitzsimmons, J. A. Aguiar, N. D. Browning, C. A. Jenkins, E. Arenholz, V. V. Mehta, U. S. Alaán, and Y. Suzuki, *Phys. Rev. Lett.* **111**, 087202 (2013).
- ⁵⁴ J. Mannhart and D. G. Schlom, *Sciences* **327**, 1607 (2010).
- ⁵⁵ J. Garcia-Barriocanal, F. Y. Bruno, A. Rivera-Calzada, Z. Sefrioui, N. M. Nemes, M. Garcia-Hernandez, J. Rubio-Zuazo, G. R. Castro, M. Varela, S. J. Pennycook, C. Leon, and J. Santamaria, *Adv. Mater.* **22**, 627 (2010).
- ⁵⁶ J. Jilili, F. Cossu, and U. Schwingenschlögl, *Scientific Reports* **5**, 13762 (2015).
- ⁵⁷ F. Cossu, J. Jilili, and U. Schwingenschlögl, *Adv. Mater. Interfaces* **1**, 1400057 (2014).
- ⁵⁸ J. Chaloupka, G. Khaliullin, *Phys. Rev. Lett.* **100**, 016404 (2008).
- ⁵⁹ T. Nguyen, V. H. Huang, T. -Y. Koo, N. -S. Lee, and H. -J. Kim, *Scientific Reports* **9**, 20145 (2019).
- ⁶⁰ H. Shishido, T. Shibauchi, K. Yasu, T. Kato, H. Kontani, T. Terashima, and Y. Matsuda, *Science* **327**, 980 (2010).
- ⁶¹ S. K. Saha, V. S. Stepanyuk, and J. Kirschner, *Physics Letters A* **378**, 3642 (2014).
- ⁶² T. Manago, T. Ono, H. Miyajima, K. Kawaguchi, and M. Sohma, *J. Phys. Soc. Japan* **68**, 3677 (1999).
- ⁶³ T. Manago, T. Ono, H. Miyajima, K. Kawaguchi, M. Sohma, *J. Phys. Soc. Japan* **68**, 334 (1999).
- ⁶⁴ T. Manago, T. Ono, H. Miyajima, K. Kawaguchi, M. Sohma, *Solid State Commun.* **109**, 621 (1999).
- ⁶⁵ T. Manago, H. Miyajima, K. Kawaguchi, M. Sohma, I. Yamaguchi, *J. Magn. Magn. Mater.* **177**, 1191 (1998).
- ⁶⁶ K. Munakata, T. H. Geballe, and M. R. Beasley, *Phys. Rev. B* **84**, 161405(R) (2011).
- ⁶⁷ M. Jiang, G. G. Batrouni, and R. T. Scalettar, *Phys. Rev. B* **86**, 195117 (2012).
- ⁶⁸ A. Zujev and P. Sengupta, *Phys. Rev. B* **88**, 094415 (2013).
- ⁶⁹ A. Euverte, F. Hebert, S. Chiesa, R. T. Scalettar, and G. G. Batrouni *Phys. Rev. Lett.* **108**, 246401 (2012).
- ⁷⁰ R. Mondaini and T. Paiva, *Phys. Rev. B* **95**, 075142 (2017).
- ⁷¹ A. Mukherjee, N. D. Patel, S. Dong, S. Johnston, A. Moreo, and E. Dagotto, *Phys. Rev. B* **90**, 205133 (2014).
- ⁷² S. Chakraborty, A. Mukherjee, and K. Pradhan, *Phys. Rev. B* **106**, 075146 (2022).
- ⁷³ A. Mukherjee, N. D. Patel, C. Bishop, and E. Dagotto, *Phys. Rev. E* **91**, 063303 (2015).
- ⁷⁴ N. D. Patel, A. Mukherjee, N. Kaushal, A. Moreo, and E. Dagotto, *Phys. Rev. Lett.* **119**, 086601 (2017).
- ⁷⁵ R. Tiwari and P. Majumdar, *Europhys. Lett.* **108**, 27007 (2014).
- ⁷⁶ S. Kumar, P. Majumdar, *Eur. Phys. J. B* **50**, 571 (2006).
- ⁷⁷ K. Pradhan and A. P. Kampf, *Phys. Rev. B* **87**, 155152 (2013).
- ⁷⁸ S. Chakraborty, S. Halder, and K. Pradhan, *Phys. Rev. B* **108**, 165110 (2023).
- ⁷⁹ S. Halder, Subrat K. Das, and K. Pradhan, *Phys. Rev. B* **108**, 235111 (2023).
- ⁸⁰ G. D. Mahan, *Quantum Many Particle Physics* (Plenum, New York, 1990).
- ⁸¹ S. Kumar and P. Majumdar, *Europhys. Lett.* **65**, 75 (2004).
- ⁸² D. Duffy and A. Moreo, *Phys. Rev. B* **55**, 12918 (1997).
- ⁸³ T. Paiva, R. T. Scalettar, C. Huscroft, and A. K. McMahan, *Phys. Rev. B* **63**, 125116 (2001).
- ⁸⁴ R. Blankenbecler, D. J. Scalapino, and R. L. Sugar, *Phys. Rev. D: Part. Fields* **24**, 2278 (1981).
- ⁸⁵ G. Rohringer, A. Toschi, A. A. Katanin, and K. Held, *Phys. Rev. Lett.* **107**, 256402 (2011).
- ⁸⁶ L. Fratino, P. Semon, M. Charlebois, G. Sordi, and A. M. S. Tremblay, *Phys. Rev. B* **95**, 235109 (2017).
- ⁸⁷ T. Sato and H. Tsunetsugu, *Phys. Rev. B* **94**, 085110 (2016).
- ⁸⁸ R. Staudt, M. Dzierzawa, and A. Muramatsu, *Eur. Phys. J. B* **17**, 411 (2000).